Electronic Supplementary Material (ESI) for Catalysis Science & Technology.

Supporting Information for:

A Mechanistic Study of Microstructure Modulation in Olefin Polymerizations using a Redox-Active Ni(II) α-Diimine Catalyst

Robert C. Chapleski, Jr., Jesse L. Kern,[‡] W. Curtis Anderson Jr.,[‡] Brian K. Long, Sharani Roy*

Department of Chemistry, University of Tennessee, Knoxville, TN 37996

Table of Contents:

Computational Section

All calculations were performed using the Gaussian09[1] software on the Advanced Computing Facility and Newton High-Performance Computing clusters at the University of Tennessee, Knoxville.

Functional validation. In order to choose a density functional theory (DFT) exchange-correlation functional that accurately describes the system under investigation, we first validated results of 10 commonly used functionals (OLYP,[2] OPBE,[3] BP86,[4] BLYP,[5] TPSS,[6] TPSSh,[6] B3LYP*,[7] B3LYP,[5, 8] M06-L,[9] M06[10]) and the cc-pVTZ basis set[11, 12] against the known (or highly evidenced) spin states and geometries for the native and reduced forms of the Ni(II) α-diimine precatalyst. For the native species **1**, the DFT method must show the spin-triplet tetrahedral d^8 Ni(II) complex to be the ground state versus the most likely alternative from crystal-field theory, a spin-singlet square-planar d^8 Ni(II) complex. For the reduced species $\mathbf{1_{red}}$, the DFT method must show a spin-doublet d^9 tetrahedral Ni(I) complex to be the ground state, based on the *g*-value of 2.32 determined by EPR and Evan's method result of 2.5 μ_B. We compare our DFT results for the spin-doublet tetrahedral species to two alternatives: spin-quartet tetrahedral and spin-doublet square-planar structures.

Relative energies as calculated from DFT are shown in Figs. S1 and S2. The native form of the precatalyst is charge-neutral whereas the reduced form of the precatalyst is anionic with a charge of -1 due to addition of an electron. For each species and functional, the electronic ground state is assigned to zero energy, and the other energies are shown relative to ground state. The functionals that give the correct prediction for **1** are TPSSh, B3LYP*, B3LYP, M06-L, and M06, and the functionals that correctly predict $\mathbf{1_{red}}$ are OLYP, OPBE, BP86, BLYP, TPSS, TPSSh, B3LYP*, and B3LYP. Three of the functionals are correct in both cases: TPSSh, B3LYP*, and B3LYP. To discern the relative accuracy of these three finalists, we compared the optimized structure of **1** to a similar crystal structure determined experimentally and reported in the work of Liu *et al.*[13] The key bonds and distances considered are shown in Table S1. TPSSh yields the least mean error and mean absolute error, and thus TPSSh is our functional of choice. The TPSSh functional has previously been shown to describe the geometries,[14-20] reaction energetics,[18-23] thermochemistry,[24, 25] and spectra[19, 26] of organometallic complexes well.

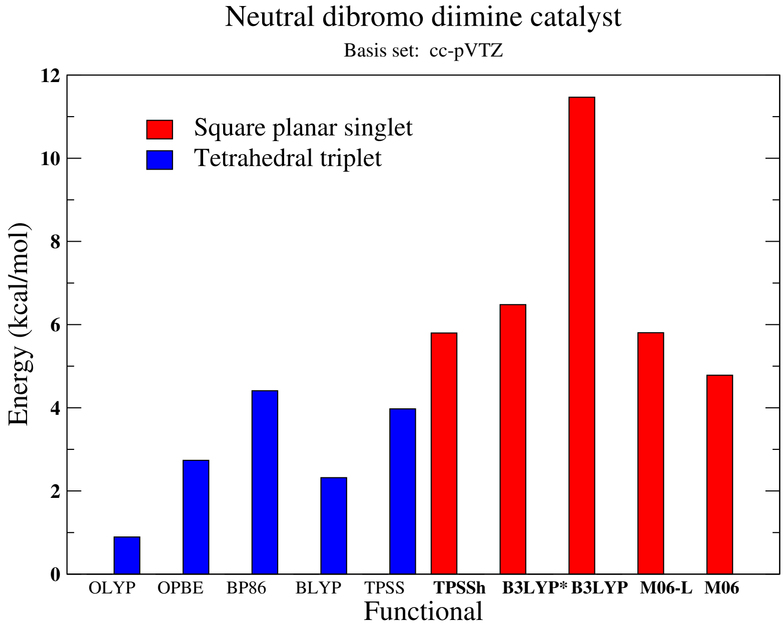

Figure S1. Functional validation for the neutral species **1**. Energies are given relative to the ground-state geometry as predicted by each functional. The experimentally observed structure is a spin-triplet tetrahedral d^8 Ni(II) complex. Functionals which give correct predictions using the cc-pVTZ basis set are shown in bold (TPSSh, B3LYP*, B3LYP, M06-L, M06).

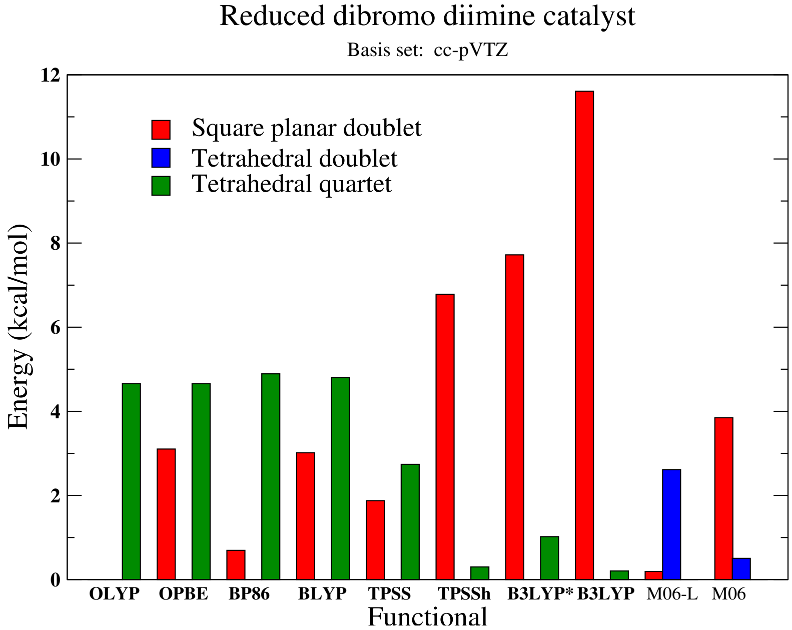

Figure S2. Functional validation for the anionic species **1**$_{\mathbf{red}}$. Energies are given relative to the ground-state geometry/spin as predicted by each functional. The experimentally observed structure is a spin-doublet tetrahedral d^9 Ni(II) complex. Functionals which give correct predictions at the cc-pVTZ basis set are shown in bold (OLYP, OPBE, BP86, BLYP, TPSS, TPSSh, B3LYP*, B3LYP).

Table S1. Literature crystal geometry and calculated structure of **1**.

Bond lengths (Å)	**Liu crystal[13]**	**B3LYP**	**B3LYP***	**TPSSh**
Ni−Br	2.323	2.367	2.359	2.341
Ni−Br	2.326	2.367	2.359	2.341
Ni−N	2.037	2.088	2.068	2.036
Ni−N	2.018	2.088	2.068	2.036
N=C	1.287	1.279	1.284	1.288
N=C	1.283	1.279	1.284	1.288
C−C	1.524	1.509	1.504	1.495
Mean error		−0.0255	−0.0180	−0.0038
Mean absolute error		0.0330	0.0247	0.0125

Effect of dispersion, solvent, and diffuse functions. Using TPSSh as our chosen functional, we evaluated the effects of adding more physically realistic corrections to the computational method. These are (*a*) Grimme's D3 dispersion scheme with Becke-Johnson parameters (D3-BJ),[27, 28] (*b*) solvent implementation using the Polarizable Continuum Model (PCM) method,[29] and (*c*) diffuse basis-set functions using the "calendar" basis sets.[30] For solvent, we used PCM toluene, and for diffuse functions, we started with the may-cc-pVTZ basis set. We use these three computational schemes, together (referred to as "full" treatment) and individually, to recalculate the three key energy differences (from the five species calculated for the functional validation).

The three energy differences, (a) ∆E(spin-singlet square-planar minus spin-triplet tetrahedral) for **1**, (b) ∆E(spin-quartet tetrahedral minus spin-doublet tetrahedral) for $\mathbf{1}_{\mathbf{red}}$, and (c) ∆E(spin-doublet square-planar minus spin-doublet tetrahedral) for $\mathbf{1}_{\mathbf{red}}$ are shown in Fig. S3 for the different treatment options versus the original TPSSh/cc-pVTZ results (labeled as "none"). The notable effects of the additional treatments are as follows: dispersion over-stabilizes the spin-quartet tetrahedral form of $\mathbf{1}_{\mathbf{red}}$, making it lower in energy than the spin-doublet tetrahedral form; PCM toluene greatly stabilizes the spin-doublet tetrahedral form of $\mathbf{1}_{\mathbf{red}}$; and diffuse functions have a very minor effect on the energy differences, even for the anionic species. We show the same energy differences, but relative to the "full" treatment that includes all three corrections, in Figs. S3 and S4. Due to the minor effect of adding the May diffuse functions, and because of the opposing nature of the effects of Grimme-D3 dispersion and PCM toluene on the energy differences, we chose to perform calculations using the TPSSh functional, the cc-pVTZ basis set, the D3-BJ dispersion method and the PCM solvent model for toluene. As a note, in Figs. 7-9, all species in the reaction pathways for the native catalyst are cationic because they are derived from **A1** and all species in the reaction pathways for the native catalyst are neutral because they are derived from $\mathbf{A1}_{\mathbf{red}}$. There are no anionic species in any of the computed reaction pathways. A comparison of the reference crystal structure of Liu *et al.*[13] with the optimized structure of **1** using this computational approach is provided in Table S2.

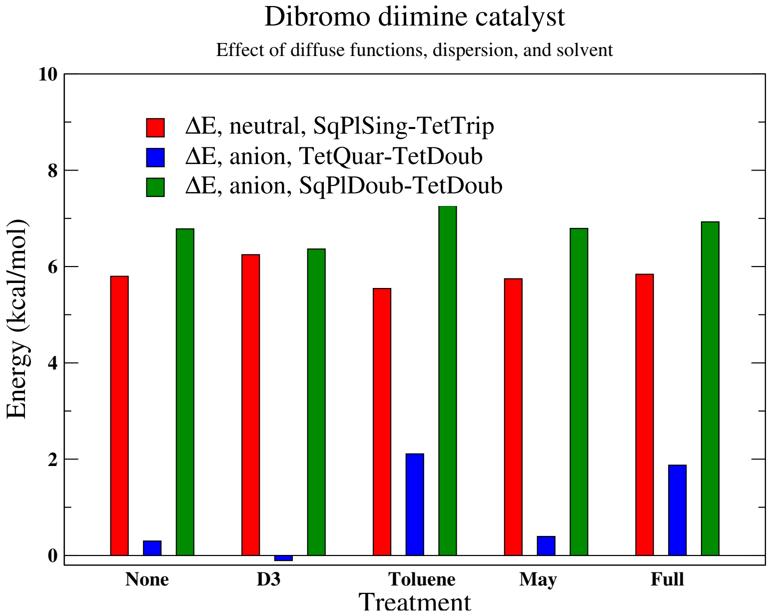

Figure S3. Effects of dispersion, solvent, diffuse functions, and “full” treatments on the three key energy differences considered for **1** and $\mathbf{1_{red}}$. All values calculated using the TPSSh functional and cc-pVTZ basis set.

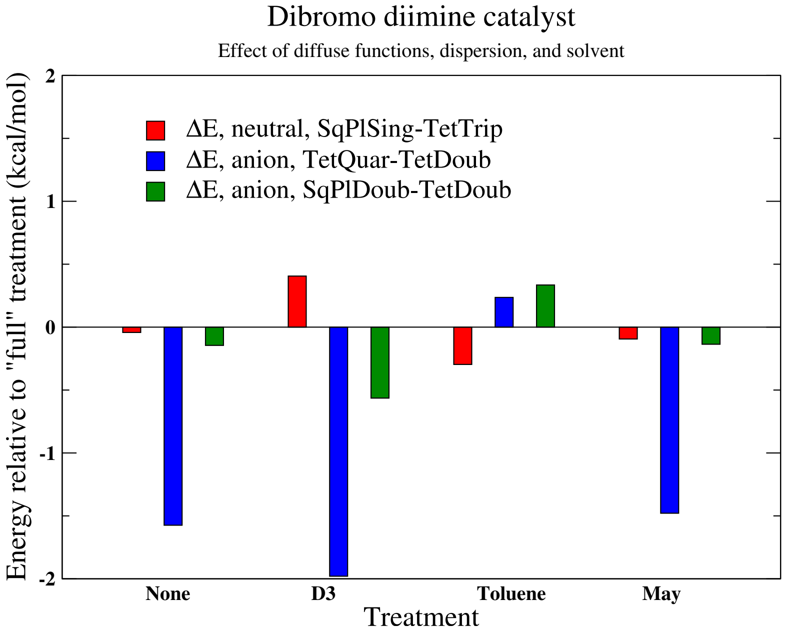

Figure S4. Effects of dispersion, solvent, and diffuse functions on the key energy differences for **1** and $\mathbf{1_{red}}$ relative to the effect of the “full” treatment, which combines all three treatments. The D3 and toluene treatments show opposite effects, relative to the “full” treatment, and May performs no better than “none”. All values calculated at the TPSSh/cc-pVTZ level of theory.

Table S2. Geometry of reference crystal structure compared to that of **1** calculated using the chosen method (*i.e.*, TPSSh/cc-pVTZ using D3-BJ dispersion and PCM toluene). The large difference in planar angle around Ni arises from the differences in ligands between the crystal structure from Liu *et al*. and **1**.

Bond lengths (Å)	**Liu crystal**[13]	**TPSSh**
Ni−Br	2.323	2.348
Ni−Br	2.326	2.348
Ni−N	2.037	2.029
Ni−N	2.018	2.029
N=C	1.287	1.285
N=C	1.283	1.285
C−C	1.524	1.491
Mean error		−0.0024
Mean absolute error		0.0147
Planar angle around Ni	80.24°	90.00°

Finally, recent work has shown that the integration grid chosen for DFT calculations can have a significant impact on resulting energies and product selectivities.[31] To probe any possible effect of the integration grid in this work, we compared the ΔG of **I-3** species (i.e., G(**I-3**$^{n\text{-pr}}$) – G(**I-3**$^{i\text{-pr}}$)) calculated using two different grids. Table S3 shows ΔG calculated using a "Fine" pruned (75,302) grid and an "Ultrafine" pruned (99,590) grid. The "Fine" pruned (75,302) grid is the default grid for Gaussian 09 calculations. As increasing the size of the integration grid results in a change in ΔG of 0.5 kcal/mol or less, we elected to proceed with the "Fine" pruned grid for the remainder of DFT calculations in this work.

Table S3. ΔG (kcal/mol) between linear and branched ethylene-addition products calculated using two different integration grids for the native and reduced catalysts.

	Fine Grid	Ultrafine Grid
Native	-0.9	-1.1
Reduced	-5.1	-5.6

Dimerization Pathway. We computationally investigated the process in which the addition of an electron to precatalyst **1** dissociates one of the Ni-Br bonds, subsequently forming an overall neutral, solvent-coordinated species, dipp-BIANNiBr(η$_2$-toluene) (**b**). This species could then dimerize to produce a different form of the reduced catalyst, dipp-BIANNi(μ-Br$_2$)Nidipp-BIAN (**c**), as is shown in Fig. S5. We began this pathway with **1**$_{\text{red}}$ coordinated to a cobaltocenium ion and an explicit toluene molecule as separated reagents. As a note, structures **a**, **b**, and **c** are Ni(I) species, and therefore could potentially give rise to the observed *g*-value of 2.32 in experimental EPR spectra. The formation of **b** from **1**$_{\text{red}}$ was calculated to be endergonic by ΔG = 17.1 kcal/mol and the final product dimer, **c**, was found to have a free energy of ΔG = 2.2 kcal/mol greater than that of monomeric **a**. The cobaltocenium cation was included in these computations to account for dissociation of the ion pair to form **b** or **c**. Based on these results, we concluded that $\mathbf{1}_{\mathbf{red}}$ (Fig. 2) was the most stable form of the reduced catalyst as indicated by the higher energies of **b** and **c** and was used for computations throughout the remainder of this work. All species along the pathway shown in Fig. S5 were calculated using TPSSh/cc-pVTZ using D3-BJ dispersion and PCM toluene, with the exception of the dimer species, **c**, the structure of which was fully optimized using the chosen method; however, due to resource limitations, vibrational frequencies and free-energy corrections at this stationary point were calculated using the cc-pVDZ basis set without empirical dispersion or implicit solvent. Further, the geometry optimization of explicit toluene resulted in a low-frequency imaginary mode ($\tilde{\nu} = 30.53i\ cm^{-1}$), as did the optimization of **b**, dipp-BIANNiBr(η2-toluene) ($\tilde{\nu} = 26.78i\ cm^{-1}$).

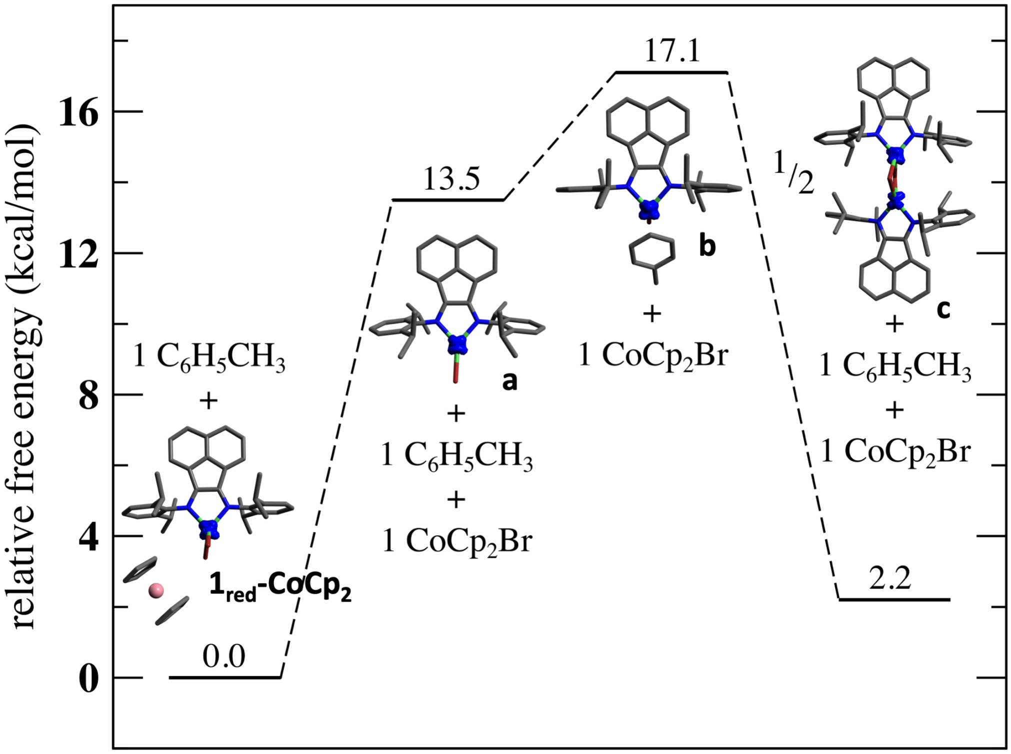

Figure S5. Relative free energies of species on the investigated pathway to a dimeric form of the reduced catalyst. $\mathbf{1}_{\mathbf{red}}$ coordinated to a cobaltocenium ion was found to be the most stable form of the reduced precatalyst. For inset structures, colors of atoms and spin densities are the same as in Fig. 2 in the main text, and hydrogen atoms have been removed for clarity.

1

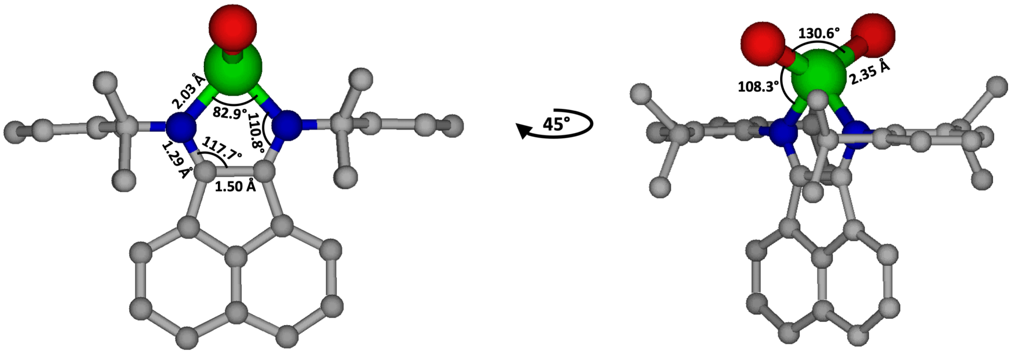

Figure S6. Structure of **1** from two different viewpoints with selected interatomic distances and bond angles identified. Same color scheme as in Fig. 7 of the main text, and hydrogen atoms have been removed for clarity.

1$_{\text{red}}$

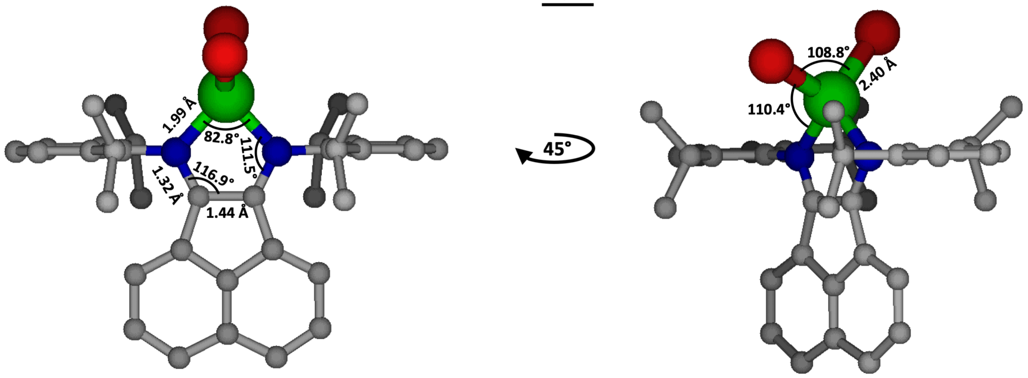

Figure S7. Structure of **1**$_{\text{red}}$ from two different viewpoints with selected interatomic distances and bond angles identified. Same color scheme as in Fig. 7 of the main text, and hydrogen atoms have been removed for clarity.

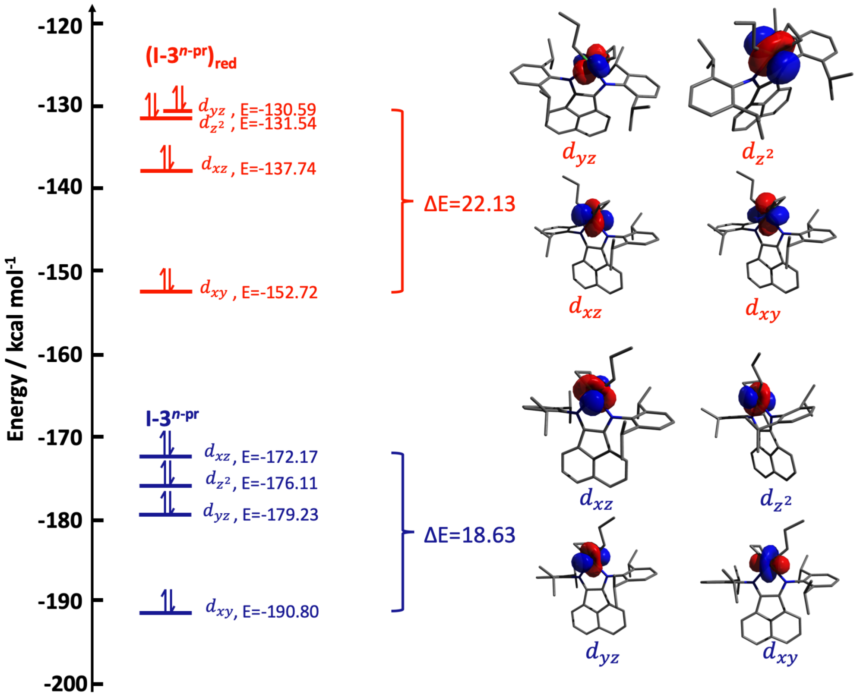

Figure S8. Energies and orbitals from DFT for the doubly-occupied nonbonding d-orbitals in **I-3$^{n\text{-pr}}$** (blue lines and text) and **(I-3$^{n\text{-pr}}$)$_{\text{red}}$** (red lines and text). Natural-bonding-orbital surfaces are shown with an isovalue of 0.03 electrons/Bohr^3, overlaying optimized molecular structures with hydrogen atoms removed for clarity. ΔE values for each species are calculated as the difference in energy between the highest- and lowest-energy nonbonding d-orbitals. An increase in ΔE upon reduction indicates greater ligand field splitting.

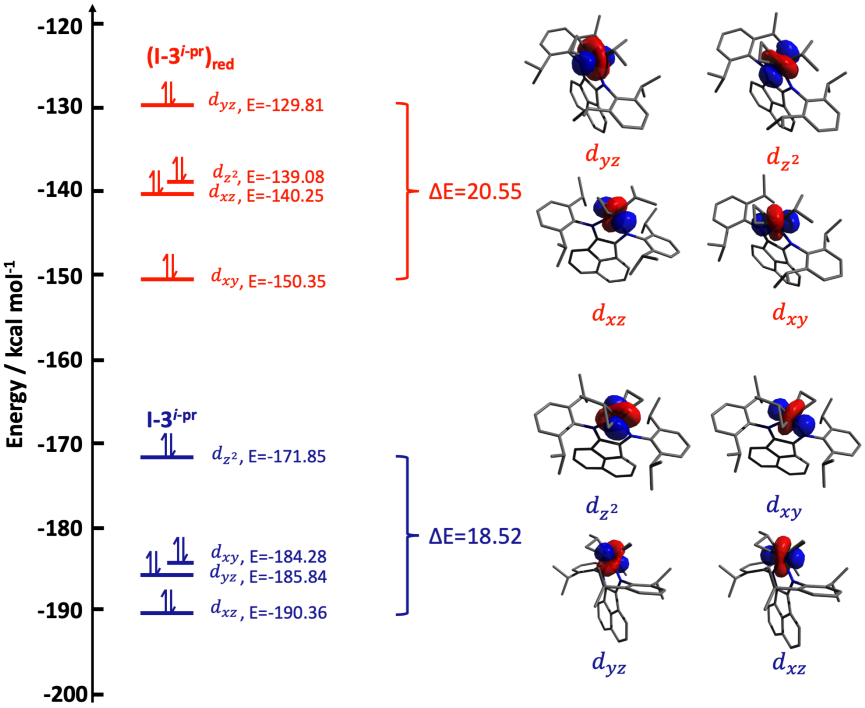

Figure S9. Energies and orbitals from DFT for the doubly-occupied nonbonding d-orbitals in **I-3$^{i\text{-pr}}$** (blue lines and text) and **(I-3$^{i\text{-pr}}$)$_{\text{red}}$** (red lines and text). Natural-bonding-orbital surfaces are shown with an isovalue of 0.03 electrons/Bohr^3, overlaying optimized molecular structures with hydrogen atoms removed for clarity. ΔE values for each species are calculated as the difference in energy between the highest- and lowest-energy nonbonding d-orbitals. An increase in ΔE upon reduction indicates greater ligand field splitting.

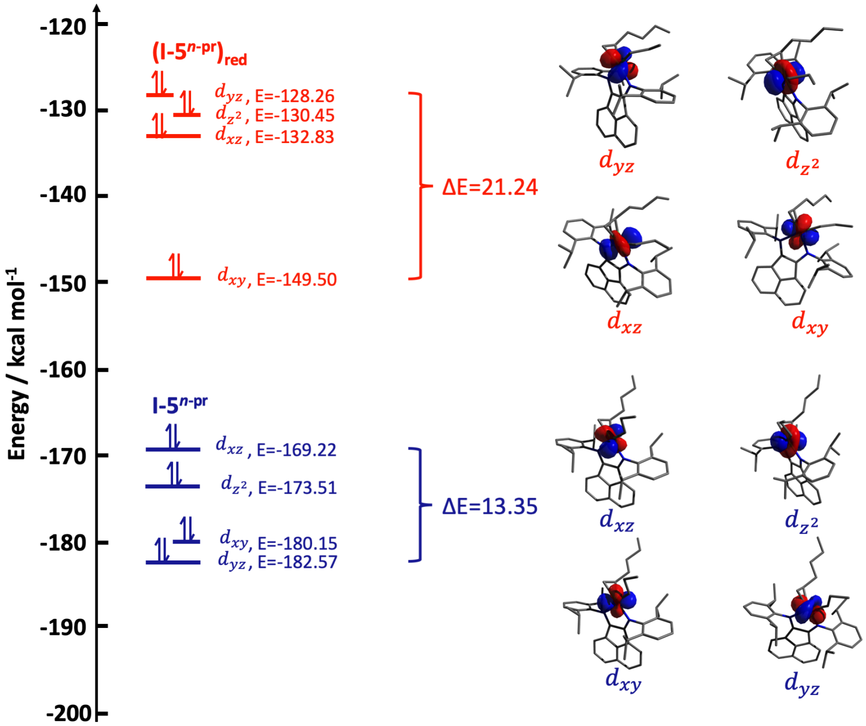

Figure S10. Energies and orbitals from DFT for the doubly-occupied nonbonding d-orbitals in **I-5$^{n\text{-pr}}$** (blue lines and text) and **(I-5$^{n\text{-pr}}$)$_{\text{red}}$** (red lines and text). Natural-bonding-orbital surfaces are shown with an isovalue of 0.03 electrons/Bohr^3, overlaying optimized molecular structures with hydrogen atoms removed for clarity. ΔE values for each species are calculated as the difference in energy between the highest- and lowest-energy nonbonding d-orbitals. An increase in ΔE upon reduction indicates greater ligand field splitting.

Remnant β-agostic interaction in I-3$^{i\text{-pr}}$. An interesting characteristic of the four **I-2** species is the β-agostic interaction between the Ni atom and a β-hydrogen atom on the propyl ligand. The four **I-2** species are shown in Fig. S11, and the interatomic distances between the Ni and H atoms involved in the β-agostic interaction are given in black, while the distances between the H atom and the propyl C atom to which it is bound are given in blue. When a second ethylene molecule is added to **I-2** to form **I-3**, this β-agostic interaction is disrupted, marked by an increase in interatomic Ni—H distance, as shown in Fig. S13 for the four **I-3** species. In three of these species, the β-agostic interaction is fully disrupted, as marked by Ni—H distances well above 2 Å, while in the fourth, **I-3$^{i\text{-pr}}$**, some semblance of the interaction remains, with an Ni—H distance of 1.84 Å. This remnant β-agostic interaction in **I-3**$^{i\text{-pr}}$ manifests in a different charge distribution around the Ni atom compared to the other three **I-3** species. Namely, the charge on the Ni atom is lower (+0.319 |e|) in **I-3**$^{i\text{-pr}}$ than in the other three species, while the charge on the propyl group is higher (+0.192 |e|). In fact, in the other three **I-3** species, the charge on the propyl group is negative. Charges of the Ni and H atoms implicated in the β-agostic interaction, as well as the net charge of the propyl group, as determined through natural bond order analysis,[32] are given in Table S4 for **I-2** species and Table S6 for **I-3** species. This difference in charge, i.e., a lower Ni charge and a higher propyl group charge implies that the remnant β-agostic interaction serves as a conduit of charge transfer from the Ni atom to the propyl group, with the result of making the Ni atom less electrophilic in **I-3**$^{i\text{-pr}}$. As a direct consequence of this decreased electrophilicity, ethylene binding is weakened, resulting in a less stable **I-3**$^{i\text{-pr}}$ product relative to the **I-2**$^{i\text{-pr}}$ precursory intermediate when compared to **I-3**$^{n\text{-pr}}$ relative to **I-2**$^{n\text{-pr}}$. No such difference in β-agostic interaction is seen at the transition state (Fig. S12 and Table S5).

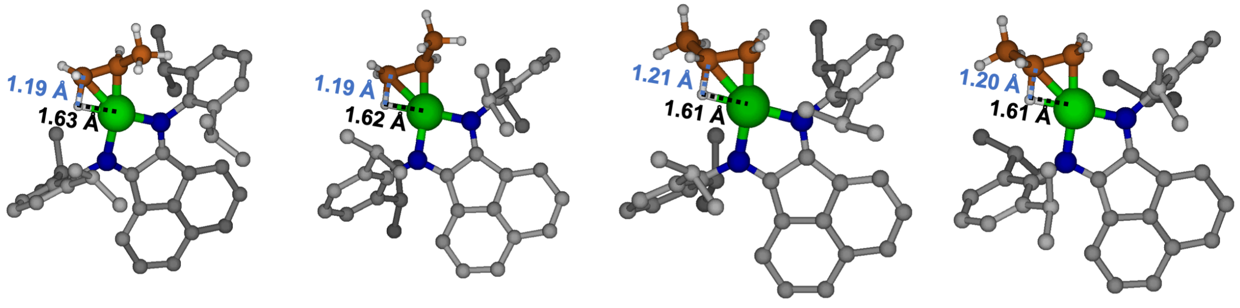

I-2$^{i\text{-pr}}$ **(I-2**$^{i\text{-pr}}$**)**$_{\text{red}}$ **I-2**$^{n\text{-pr}}$ **(I-2**$^{n\text{-pr}}$**)**$_{\text{red}}$

Figure S11. DFT-optimized structures of **I-2**$^{i\text{-pr}}$**, (I-2**$^{i\text{-pr}}$**)**$_{\text{red}}$**, I-2**$^{n\text{-pr}}$, and **(I-2**$^{n\text{-pr}}$**)**$_{\text{red}}$, with selected Ni—H interatomic distances labeled in black and C—H distances labeled in blue, in Angstroms, to emphasize the β-agostic interaction. Same atom color scheme as in Fig. 7 of main body of text.

Table S4. Atomic charges from natural bond order analysis for the Ni and H atoms indicated by interatomic distances in Fig. S11 as well as the net charge of the propyl fragment.

Charge (|e|)	**I-2**$^{i\text{-pr}}$	**(I-2**$^{i\text{-pr}}$**)**$_{\text{red}}$	**I-2**$^{n\text{-pr}}$	**(I-2**$^{n\text{-pr}}$**)**$_{\text{red}}$
Ni	+0.495	+0.435	+0.480	+0.439
H	+0.185	+0.186	+0.170	+0.171
propyl	+0.101	+0.010	+0.082	-0.013

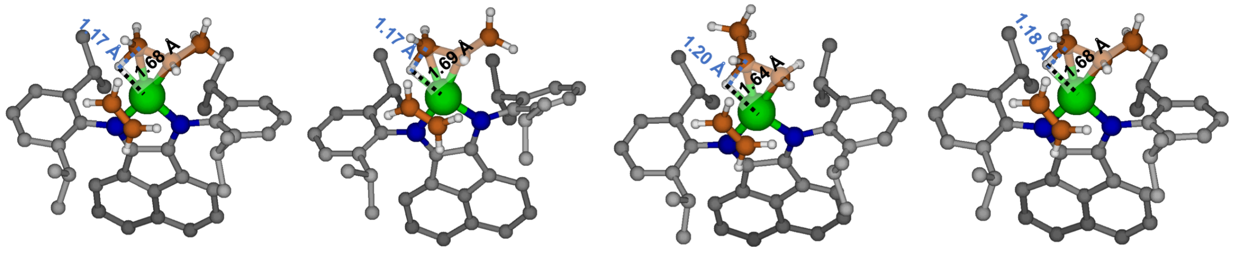

TS-2$^{i\text{-pr}}$ **(TS-2$^{i\text{-pr}}$)$_{\text{red}}$** **TS-2$^{n\text{-pr}}$** **(TS-2$^{n\text{-pr}}$)$_{\text{red}}$**

Figure S12. DFT-optimized structures of **TS-2$^{i\text{-pr}}$, (TS-2$^{i\text{-pr}}$)$_{\text{red}}$, TS-2$^{n\text{-pr}}$**, and **(TS-2$^{n\text{-pr}}$)$_{\text{red}}$**, with selected Ni—H interatomic distances labeled in black and C—H distances labeled in blue, in Angstroms, to emphasize the β-agostic interaction which remains from precursor **I-2** species. Same atom color scheme as in Fig. 7 of main body of text.

Table S5. Atomic charges from natural bond order analysis for the Ni and H atoms indicated by interatomic distances in Fig. S12 as well as the net charge of the propyl fragment

Atomic Charge (|e|)	**TS-2$^{i\text{-pr}}$**	**(TS-2$^{i\text{-pr}}$)$_{\text{red}}$**	**TS-2$^{n\text{-pr}}$**	**(TS-2$^{n\text{-pr}}$)$_{\text{red}}$**
Ni	+0.479	+0.412	+0.495	+0.429
H	+0.189	+0.196	+0.167	+0.172
propyl	+0.099	+0.018	+0.077	-0.007

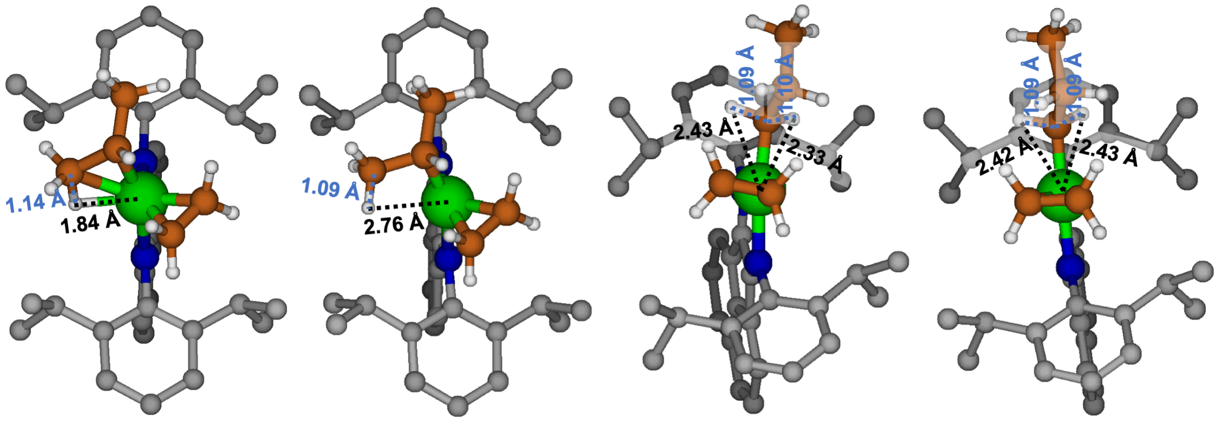

I-3$^{i\text{-pr}}$ **(I-3$^{i\text{-pr}}$)$_{\text{red}}$** **I-3$^{n\text{-pr}}$** **(I-3$^{n\text{-pr}}$)$_{\text{red}}$**

Figure S13. DFT-optimized structures of **I-3$^{i\text{-pr}}$, (I-3$^{i\text{-pr}}$)$_{\text{red}}$, I-3$^{n\text{-pr}}$**, and **(I-3$^{n\text{-pr}}$)$_{\text{red}}$**, with selected Ni—H interatomic distances labeled in black and C—H distances labeled in blue, in Angstroms, to emphasize the β-agostic interaction which remains from precursor **I-2** species only in **I-3$^{i\text{-pr}}$**. Same atom color scheme as in Fig. 7 of main body of text.

Table S6. Atomic charges from natural bond order analysis for the Ni and H atoms indicated by interatomic distances in Fig. S13 as well as the net charge of the propyl fragment.

Atomic Charge (|e|)	**I-3$^{i\text{-pr}}$**	**(I-3$^{i\text{-pr}}$)$_{\text{red}}$**	**I-3$^{n\text{-pr}}$**	**(I-3$^{n\text{-pr}}$)$_{\text{red}}$**
Ni	+0.319	+0.470	+0.509	+0.476
H	+0.213	+0.202	+0.197, +0.191	+0.185, +0.187
propyl	+0.192	-0.089	-0.085	-0.176

Table S7. Differences in Gibbs free energy, along with enthalpic and entropic contributions, and electronic energy for ethylene- or hexene-added products in Figs. 8 and 9. All energies are in kcal/mol and thermodynamic quantities are calculated at a temperature of 298.15 K.

Products	ΔG	ΔH	TΔS	ΔE
I-3$^{i\text{-pr}}$ - I-3$^{n\text{-pr}}$	0.9	-0.6	-1.5	-0.2
(I-3$^{i\text{-pr}}$)$_{\text{red}}$ - (I-3$^{n\text{-pr}}$)$_{\text{red}}$	5.1	3.2	-1.9	3.3
I-5$^{n\text{-pr}}$ - I-3$^{n\text{-pr}}$	-0.1	-1.1	-1.0	-1.2
(I-5$^{n\text{-pr}}$)$_{\text{red}}$ - (I-3$^{n\text{-pr}}$)$_{\text{red}}$	1.7	-1.6	-3.3	-1.8

Experimental Methods and Materials

General Methods and Materials. All reactions were performed under an inert nitrogen atmosphere using an MBraun UniLab glovebox or using standard Schlenk techniques, unless otherwise noted. All solvents were dried using an Innovative Technologies PureSolv Solvent Purification System and degassed via three freeze-pump-thaw cycles. Catalyst **1** was prepared according to literature.[33] PMAO-IP (2.3 M in toluene) was purchased from Akzo Nobel and used as received. CD_2Cl_2 was dried over activated molecular sieves (4Å) and degassed by three freeze-pump-thaw cycles prior to use. All other reagents were purchased from commercial vendors and used without further purification. Polyethylene ^{1}H spectra were recorded at 20 °C on a Varian 500 MHz NMR in $CDCl_3$ or on a Bruker 400 MHz NMR in $C_2D_2Cl_4$. Evans Method experiments were performed according to literature procedures.[34] UV-Vis measurements were obtained using an Ocean Optics USB4000-UV-Vis spectrophotometer. EPR measurements were obtained on a Bruker EMX (X-band) EPR spectrometer.

General ethylene polymerization conditions. To a Fisher-Porter bottle was added catalyst **1** (10 µmol) dissolved in dichloromethane (2 mL), toluene (50 mL), and a magnetic stir bar. The bottle was sealed and placed in an oil bath at the desired temperature. The vessel was pressurized with ethylene (75 psi) and allowed to equilibrate under constant pressure for 10 minutes with stirring. The appropriate amount of trimethylaluminum (TMA) solution (1.0 M in toluene) or PMAO-IP (2.3 M in toluene) was injected to initiate polymerization and was stirred continuously for the desired time. The polymerization was quenched via the addition of MeOH (10 mL), and the polymer was precipitated by adding excess acidic MeOH (5% HCl in MeOH), and dried in a vacuum oven to constant weight. Polymerizations using reductant were performed using the same conditions, except cobaltocene (10 μmol, 1 equiv.) was added to the DCM solution that catalyst **1** was dissolved in.

NMR Spectra

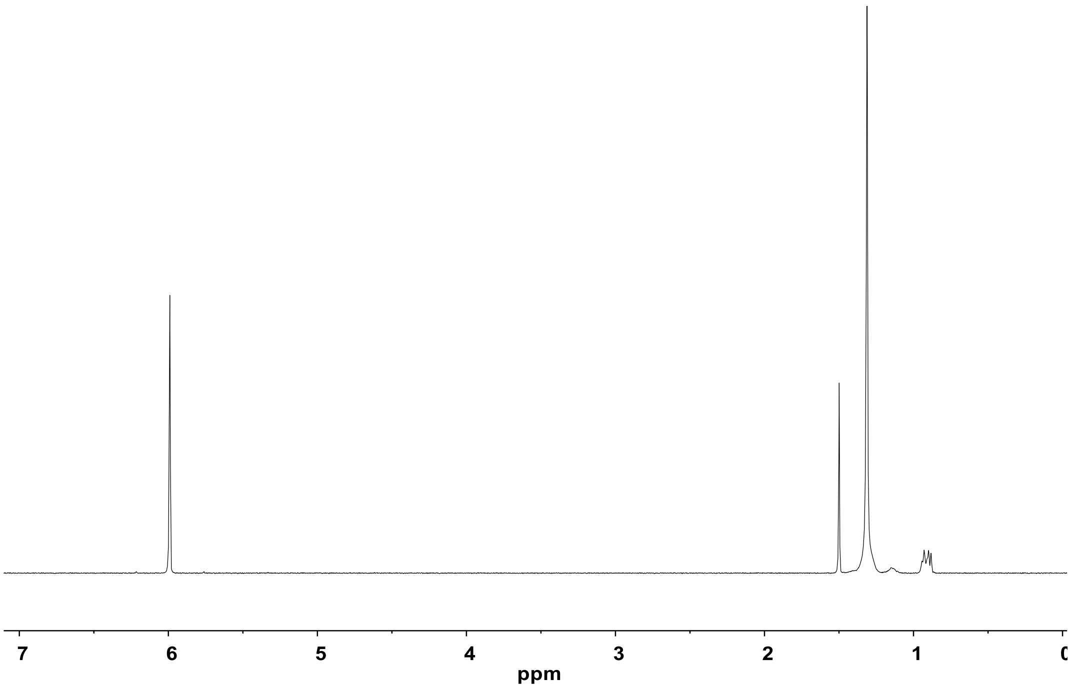

Figure S14. Representative ^{1}H NMR of polyethylene produced using catalyst **1** + 200 eq. TMA.

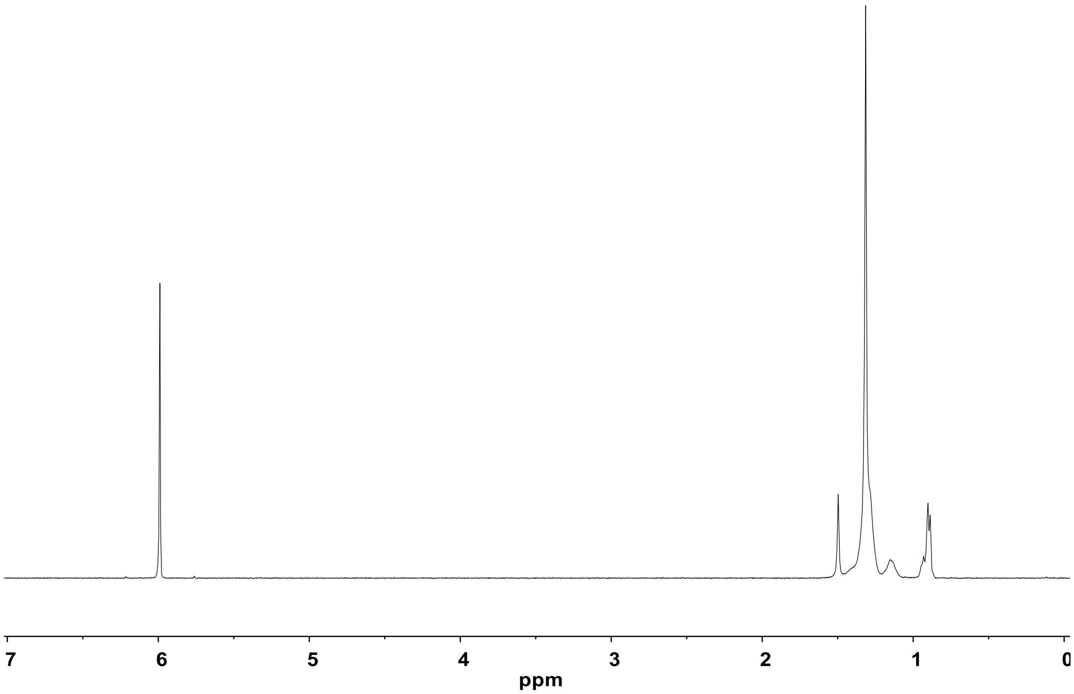

Figure S15. Representative ^{1}H NMR of polyethylene produced using catalyst **1** + 500 eq. PMAO-IP.

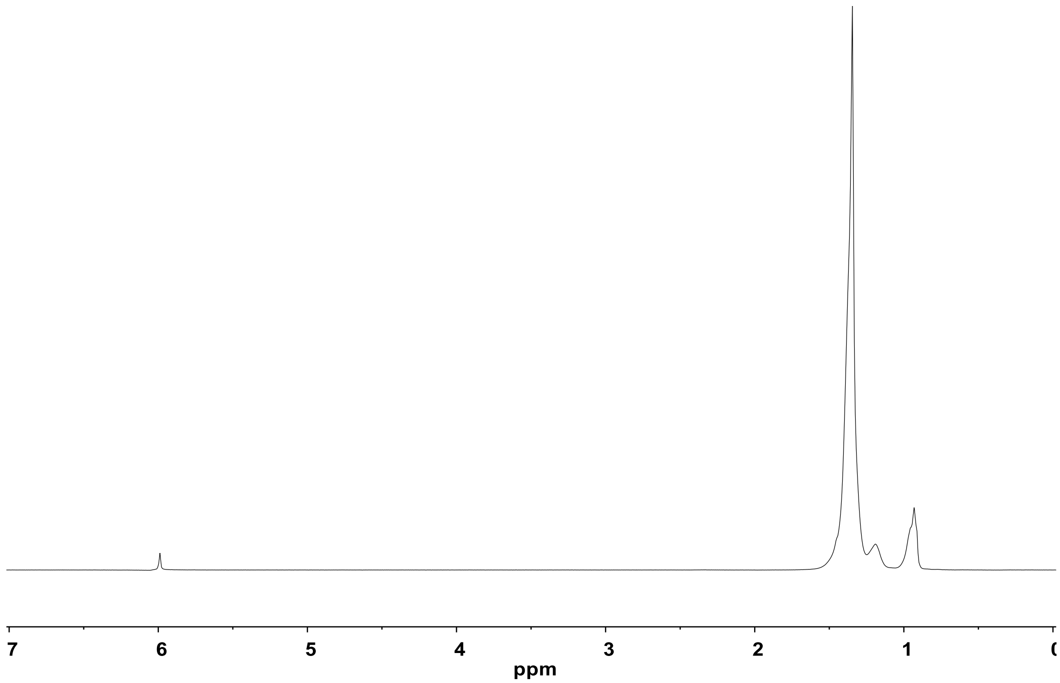

Figure S16. Representative ^{1}H NMR of polyethylene produced using catalyst **1** + 1 eq. cobaltocene + 500 eq. PMAO-IP.

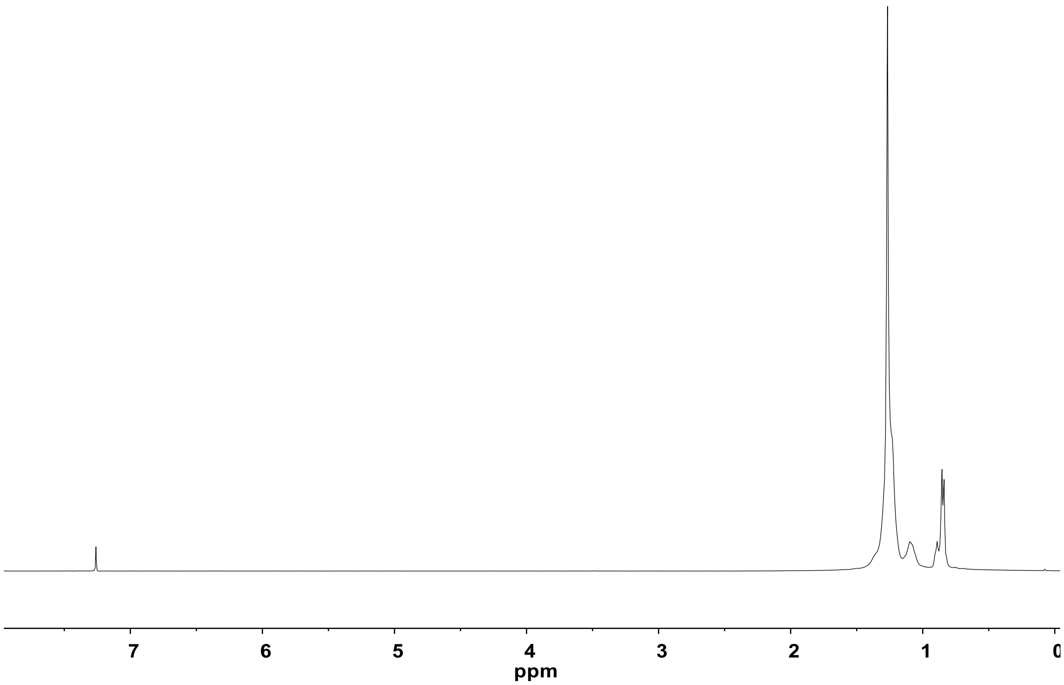

Figure S17. Representative ^{1}H NMR of polyethylene produced using catalyst **1** + 200 eq. TMA + 500 eq. MAO.

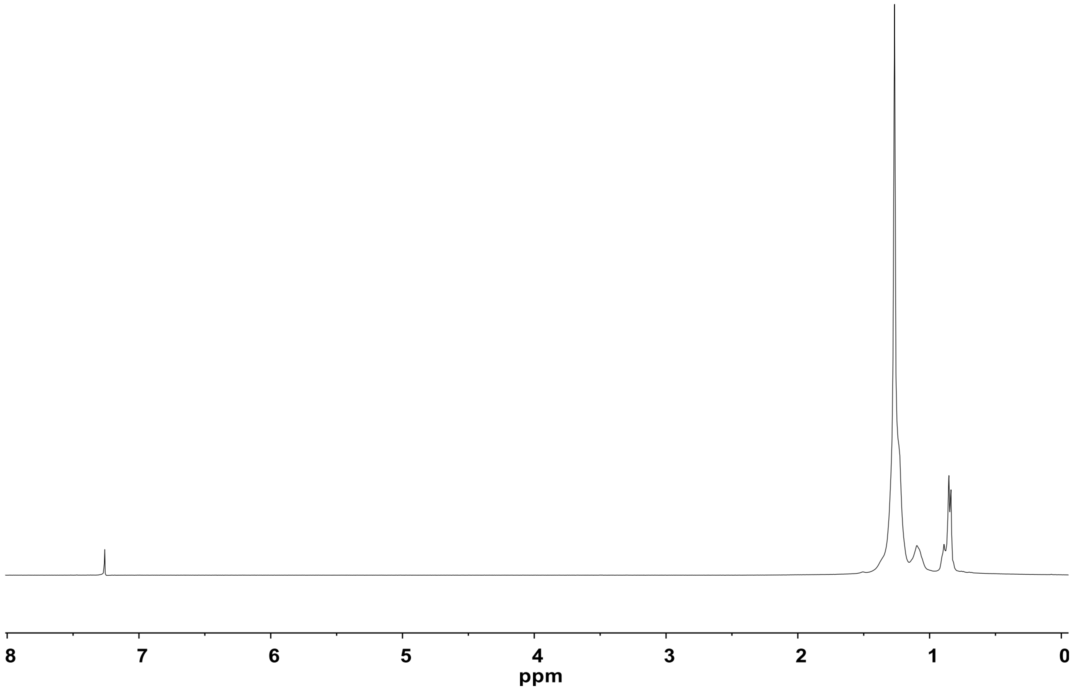

Figure S18. Representative ^{1}H NMR of polyethylene produced using catalyst **1** + 1 eq. cobaltocene, 200 eq. TMA, and 500 eq. TMA.

References for Supporting Information

1. Frisch, M. J.; Trucks, G. W.; Schlegel, H. B.; Scuseria, G. E.; Robb, M. A.; Cheeseman, J. R.; Scalmani, G.; Barone, V.; Mennucci, B.; Petersson, G. A.; Nakatsuji, H.; Caricato, M.; Li, X.; Hratchian, H. P.; Izmaylov, A. F.; Bloino, J.; Zheng, G.; Sonnenberg, J. L.; Hada, M.; Ehara, M.; Toyota, K.; Fukuda, R.; Hasegawa, J.; Ishida, M.; Nakajima, T.; Honda, Y.; Kitao, O.; Nakai, H.; Vreven, T.; Montgomery Jr., J. A.; Peralta, J. E.; Ogliaro, F.; Bearpark, M. J.; Heyd, J. J.; Brothers, E. N.; Kudin, K. N.; Staroverov, V. N.; Keith, T. A.; Kobayashi, R.; Normand, J.; Raghavachari, K.; Rendell, A. P.; Burant, J. C.; Iyengar, S. S.; Tomasi, J.; Cossi, M.; Rega, N.; Millam, J. M.; Klene, M.; Knox, J. E.; Cross, J. B.; Bakken, V.; Adamo, C.; Jaramillo, R.; Gomperts, R.; Stratmann, R. E.; Yazyev, O.; Austin, A. J.; Cammi, R.; Pomelli, C.; Ochterski, J. W.; Martin, R. L.; Morokuma, K.; Zakrzewski, V. G.; Voth, G. A.; Salvador, P.; Dannenberg, J. J.; Dapprich, S.; Daniels, A. D.; Farkas, O.; Foresman, J. B.; Ortiz, J. V.; Cioslowski, J.; Fox, D. J. *Gaussian 09 Rev. D.01*, Wallingford, CT, 2013.
2. Cohen, A. J.; Handy, N. C., Dynamic Correlation. *Molecular Physics* **2001,** *99* (7), 607-615.
3. Swart, M.; Ehlers, A. W.; Lammertsma *, K., Performance of the OPBE Exchange-Correlation Functional. *Molecular Physics* **2004,** *102* (23-24), 2467-2474.
4. Becke, A. D., Density-Functional Exchange-Energy Approximation with Correct Asymptotic Behavior. *Physical Review A* **1988,** *38* (6), 3098-3100.
5. Lee, C.; Yang, W.; Parr, R. G., Development of the Colle-Salvetti Correlation-Energy Formula into a Functional of the Electron Density. *Physical Review B* **1988,** *37* (2), 785-789.
6. Tao, J.; Perdew, J. P.; Staroverov, V. N.; Scuseria, G. E., Climbing the Density Functional Ladder: Nonempirical Meta--Generalized Gradient Approximation Designed for Molecules and Solids. *Physical Review Letters* **2003,** *91* (14), 146401.
7. Reiher, M.; Salomon, O.; Artur Hess, B., Reparameterization of Hybrid Functionals Based on Energy Differences of States of Different Multiplicity. *Theoretical Chemistry Accounts* **2001,** *107* (1), 48-55.
8. Becke, A. D., Density-Functional Thermochemistry. III. The Role of Exact Exchange. *The Journal of Chemical Physics* **1993,** *98* (7), 5648-5652.
9. Zhao, Y.; Truhlar, D. G., A New Local Density Functional for Main-Group Thermochemistry, Transition Metal Bonding, Thermochemical Kinetics, and Noncovalent Interactions. *The Journal of Chemical Physics* **2006,** *125* (19), 194101.
10. Zhao, Y.; Truhlar, D. G., The M06 Suite of Density Functionals for Main Group Thermochemistry, Thermochemical Kinetics, Noncovalent Interactions, Excited States, and Transition Elements: Two New Functionals and Systematic Testing of Four M06-Class Functionals and 12 Other Functionals. *Theoretical Chemistry Accounts* **2008,** *120* (1), 215-241.
11. Dunning Jr., T. H., Gaussian Basis Sets for Use in Correlated Molecular Calculations. I. The Atoms Boron through Neon and Hydrogen. *The Journal of Chemical Physics* **1989,** *90* (2), 1007-1023.
12. Kendall, R. A.; Dunning Jr., T. H.; Harrison, R. J., Electron Affinities of the First-Row Atoms Revisited. Systematic Basis Sets and Wave Functions. *The Journal of Chemical Physics* **1992,** *96* (9), 6796-6806.
13. Liu, Q.; Zhang, W.; Jia, D.; Hao, X.; Redshaw, C.; Sun, W.-H., 2-{2,6-Bis[bis(4-fluorophenyl)methyl]-4-chlorophenylimino}-3-aryliminobutylnickel(II) bromide Complexes: Synthesis, Characterization, and Investigation of their Catalytic Behavior. *Applied Catalysis A: General* **2014,** *475*, 195-202.
14. Csonka, G. I.; Perdew, J. P.; Ruzsinszky, A., Global Hybrid Functionals: A Look at the Engine under the Hood. *Journal of Chemical Theory and Computation* **2010,** *6* (12), 3688-3703.
15. Bühl, M.; Kabrede, H., Geometries of Transition-Metal Complexes from Density-Functional Theory. *Journal of Chemical Theory and Computation* **2006,** *2* (5), 1282-1290.

16. Peverati, R.; Truhlar Donald, G., Quest for a Universal Density Functional: the Accuracy of Density Functionals Across a Broad Spectrum of Databases in Chemistry and Physics. *Philosophical Transactions of the Royal Society A: Mathematical, Physical and Engineering Sciences* **2014,** *372* (2011), 20120476.

17. Bühl, M.; Reimann, C.; Pantazis, D. A.; Bredow, T.; Neese, F., Geometries of Third-Row Transition-Metal Complexes from Density-Functional Theory. *Journal of Chemical Theory and Computation* **2008,** *4* (9), 1449-1459.

18. Rappoport, D., Crawford, N. R., Furche, F., Burke, K., Approximate Density Functionals: Which Should I Choose? In *Encyclopedia of Inorganic and Bioinorganic Chemistry*, 2011.

19. Staroverov, V. N.; Scuseria, G. E.; Tao, J.; Perdew, J. P., Comparative Assessment of a New Nonempirical Density Functional: Molecules and Hydrogen-Bonded Complexes. *The Journal of Chemical Physics* **2003,** *119* (23), 12129-12137.

20. Schultz, N. E.; Zhao, Y.; Truhlar, D. G., Density Functionals for Inorganometallic and Organometallic Chemistry. *The Journal of Physical Chemistry A* **2005,** *109* (49), 11127-11143.

21. Cramer, C. J.; Truhlar, D. G., Density Functional Theory for Transition Metals and Transition Metal Chemistry. *Physical Chemistry Chemical Physics* **2009,** *11* (46), 10757-10816.

22. Weymuth, T.; Couzijn, E. P. A.; Chen, P.; Reiher, M., New Benchmark Set of Transition-Metal Coordination Reactions for the Assessment of Density Functionals. *Journal of Chemical Theory and Computation* **2014,** *10* (8), 3092-3103.

23. Furche, F.; Perdew, J. P., The Performance of Semilocal and Hybrid Density Functionals in 3d Transition-Metal Chemistry. *The Journal of Chemical Physics* **2006,** *124* (4), 044103.

24. Neese, F., Prediction of Molecular Properties and Molecular Spectroscopy with Density Functional Theory: From Fundamental Theory to Exchange-Coupling. *Coordination Chemistry Reviews* **2009,** *253* (5), 526-563.

25. Harvey, J. N., On the Accuracy of Density Functional Theory in Transition Metal Chemistry. *Annual Reports Section "C" (Physical Chemistry)* **2006,** *102* (0), 203-226.

26. Kossmann, S.; Kirchner, B.; Neese, F., Performance of Modern Density Functional Theory for the Prediction of Hyperfine Structure: Meta-GGA and Double Hybrid Functionals. *Molecular Physics* **2007,** *105* (15-16), 2049-2071.

27. Grimme, S.; Antony, J.; Ehrlich, S.; Krieg, H., A Consistent and Accurate Ab Initio Parametrization of Density Functional Dispersion Correction (DFT-D) for the 94 Elements H-Pu. *The Journal of Chemical Physics* **2010,** *132* (15), 154104.

28. Grimme, S.; Ehrlich, S.; Goerigk, L., Effect of the Damping Function in Dispersion Corrected Density Functional Theory. *Journal of Computational Chemistry* **2011,** *32* (7), 1456-1465.

29. Tomasi, J.; Mennucci, B.; Cammi, R., Quantum Mechanical Continuum Solvation Models. *Chemical Reviews* **2005,** *105* (8), 2999-3094.

30. Papajak, E.; Zheng, J.; Xu, X.; Leverentz, H. R.; Truhlar, D. G., Perspectives on Basis Sets Beautiful: Seasonal Plantings of Diffuse Basis Functions. *Journal of Chemical Theory and Computation* **2011,** *7* (10), 3027-3034.

31. Andrea N., B.; Steven, W., *Popular Integration Grids Can Result in Large Errors in DFT-Computed Free Energies*. 2019.

32. Reed, A. E.; Weinstock, R. B.; Weinhold, F., Natural Population Analysis. *The Journal of Chemical Physics* **1985,** *83* (2), 735-746.

33. Johnson, L. K.; Killian, C. M.; Brookhart, M., New Pd(II)- and Ni(II)-Based Catalysts for Polymerization of Ethylene and .alpha.-Olefins. *Journal of the American Chemical Society* **1995,** *117* (23), 6414-6415.

34. Evans, D. F., 400. The Determination of the Paramagnetic Susceptibility of Substances in Solution by Nuclear Magnetic Resonance. *Journal of the Chemical Society (Resumed)* **1959,** (0), 2003-2005.